Rotation Speed Sensing with mmWave Radar

Rong Ding, Haiming Jin†, Dingman Shen
Shanghai Jiao Tong University, Shanghai, China
Email: {dingrong, jinhaiming, 631322231}@sjtu.edu.cn

***Abstract*—Machines with rotary parts are prevalent in industrial systems and our daily lives. Rotation speed measurement is a crucial task for monitoring machinery health. Previous approaches for rotation speed sensing are constrained by limited operation distance, strict requirement for illumination, or strong dependency on the target object's light reflectivity. In this work, we propose mRotate, a practical mmWave radar-based rotation speed sensing system liberated from all the above constraints. Specifically, mRotate separates the target signal reflected by the rotating object from the mixed reflection signals, extracts the high-quality rotation related features, and accurately obtains the rotation speed through the customized radar sensing mode and algorithm design. We implement mRotate on a commercial mmWave radar and extensively evaluate it in both lab environments and in a machining workshop for field tests. mRotate achieves an MAPE of 0.24% in accuracy test, which is 38% lower than that produced by the baseline device, a popular commercial laser tachometer. Besides, our experiments show that mRotate can measure a spindle whose diameter is only 5mm, maintain a high accuracy with a sensing distance as far as 2.5m, and simultaneously measure the rotation speeds of multiple objects.**

I. Introduction

Machines with rotary parts play significant roles in not only our daily lives, but also various industrial fields (e.g., machining, automobile, aviation). Accurate and safe rotation speed sensing is of great importance for monitoring machinery health. Operators in machining workshops are required to regularly check the rotation speeds of the spindles to monitor their operation statuses [1]. Checking the rotation speeds of the wheels has become a standard item for car inspection [2]. Apart from the industrial applications, the rotation speeds of the electric motors in washing machines and air conditioners are used to diagnose the causes of anomalies [3].

Thus far, a series of sensing techniques have been exploited to develop different types of rotation speed sensors (i.e., tachometers), which can be categorized into contact-based and contactless ones. Specifically, the contact-based tachometers [4] are physically attached to the spinning shaft of the target object, which restrains the distance between the operator and the rotating object and incurs safety risks. Existing contactless tachometers utilize electromagnetic or optical signals to sense the rotation speed. Among them, the electromagnetic-based methods [5, 6] apply the electrostatic or hall-effect sensors to detect the changes of the electromagnetic field caused by the rotation. However, these approaches have very limited sensing distances which are typically less than 10cm. The optical-based approaches [7–13] utilize optical sensors, such as cameras and laser receivers, for rotation speed sensing. However, camera-based tachometers have strict requirements for the illumination conditions. The laser tachometers [4] fail to work, if the target object is highly reflective. In such case, the laser tachometers cannot distinguish the laser pulse reflected by its reflective tag from those reflected by the object.

In this paper, we propose *mRotate*, a mmWave radar-based system that can accurately sense the rotation speed of the target object from a safe distance, and is robust to the illumination conditions and the target object's light reflectivity. Among all the mmWave radars, we adopt the commercial TI IWR1443 frequency-modulated continuous wave (FMCW) radar. Thanks to the over 77GHz high operation frequencies, the radar's signal is sensitive to the rotation incurred displacement on the target object's surface. Besides, the over 1e3Hz high chirp rate enables the radar to timely capture the rapid signal variations caused by high speed rotation. In what follows, we elaborate on the challenges of designing mRotate, as well as our approaches that address them.

In real practice, the rotating object is surrounded by other reflectors in the environment, and the received signal of the radar is a mixture of the signals reflected by both the rotating object and other reflectors. Thus, the first challenge is to extract our target signal reflected by the rotating object from the complicated mixed signals. To address this challenge, we utilize the unique property of the target signal that varies periodically as the object rotates. Based on that observation, we propose the *rotating object discovery* mechanism, which first separates the signals based on their propagation distances through the Range-FFT operation, and then accurately selects our target signal by discovering the one with the periodic varying property through checking the existence of distinct peaks in its autocorrelation series.

The second challenge is that, when we measure the rotation speed of roughly centrosymmetric objects (e.g., wheels, fans), the aliasing problem could mislead us to get the wrong rotation speed. Specifically, the signals reflected by the centrosymmetric rotating parts are highly similar and show an aliasing period which is easy to be confused with the rotation period. We resolve such challenge by designing the *aliasing elimination* mechanism, which employs *chirp decomposition* to obtain multiple descriptions of the rotating object, and carefully aggregates the descriptions through *feature aggregation* to generate aliasing free signal feature *group sum value (GSV)*. Our design of the GSV ensures that it significantly amplifies the difference between the centrosymmetric rotating parts, and thus makes the aliasing period disappear in the GSV series.

Meanwhile, note that the radar commonly generates chirps following a fixed chirp generation frequency in most of the common sensing applications. However, we realize that only relying on the radar's output data collected under such a

†Corresponding author.
This work was supported by NSF China (No. U20A20181, U21A20519).

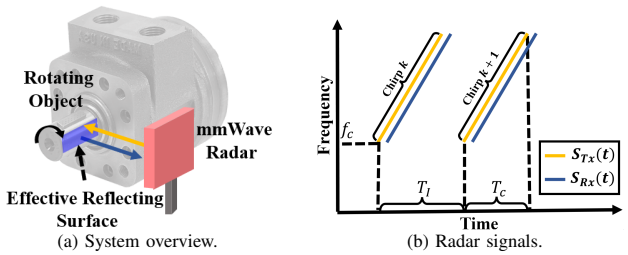

(a) System overview. (b) Radar signals.

Figure 1: Rotation speed measurement with mmWave radar.

fixed chirp generation frequency will yield multiple rotation speed candidates rather than a single accurate solution. To solve this challenge, we propose the *chirp frequency hopping* mechanism that sets the radar to transmit chirps under multiple chirp generation frequencies to obtain multiple observations of the rotating object. Our meticulously designed *rotation speed search* algorithm then carefully explores the rotation speed search space and accurately pinpoints the rotation speed which is the one that aligns with the most observations.

In summary, this paper makes the following contributions.

- We design and implement a novel mmWave radar-based rotation speed sensing system, named as mRotate, which enables accurate rotation speed sensing from a safe distance, and is robust to the illumination conditions and the target object's light reflectivity.
- Technically, we propose a series of novel approaches that (i) separate the signal reflected by the rotating object from the complicated mixed reflection signal, (ii) generate the aliasing free signal features to enable accurate rotation speed sensing for centrosymmetric objects, and (iii) pinpoint the accurate rotation speed through customized radar sensing mode and algorithm design.
- We conduct extensive experiments to evaluate mRotate on a variety of rotating objects in both lab environments and field tests. mRotate achieves an MAPE of only **0.24%** for accuracy test in lab environments, which is 38% lower than that produced by the baseline device, a popular commercial laser tachometer. Meanwhile, mRotate can measure the rotation speed of a small spindle whose diameter is only **5mm**, achieve low errors from a sensing distance as far as **2.5m**, and simultaneously obtain the rotation speeds of **multiple objects** in the field tests.

II. Preliminaries

In this section, we first introduce the basic signal propagation model of using mmWave radar for rotation speed sensing. The radar transmits FMCW chirps to the target object to sense its rotation speed. The transmitted signal of the k-th chirp is

$$S_{Tx}(t) = \exp\big(j(2\pi f_c t + \pi L t^2)\big), \tag{1}$$

where f_c is the chirp starting frequency, L is the chirp slope, and $t \in [(k-1)T_I, (k-1)T_I + T_c]$ with T_I denoting the time interval between the generation of two consecutive chirps and T_c denoting the duration of one chirp.

As illustrated in Fig. 1a, we refer to the part of the target object's surface that reflects the radar signal as the *effective reflecting surface (ERS)*. The signal reflected by the ERS is

$$S_{Rx}(t) = \alpha(t) S_{Tx}\big(t - 2R(t)/c\big), \tag{2}$$

where $R(t)$ is the ERS-radar distance, and $\alpha(t) = \beta(R(t))\gamma(t)$ is the path loss with $\beta(R(t))$ denoting the propagation loss and $\gamma(t)$ denoting the reflection loss. Note that $R(t)$ is not only time-varying but also periodic, because the target object's rotation incurs a periodic change to the shape of the ERS, and further to $R(t)$. Besides, $\alpha(t)$ is also periodic, because $\beta(R(t))$ changes with $R(t)$, and $\gamma(t)$ is periodic as well. After receiving $S_{Rx}(t)$, the radar applies a mixer on $S_{Tx}(t)$ and $S_{Rx}(t)$ to obtain the beat frequency (BF) signal

$$s(t) = S^*_{Tx}(t) S_{Rx}(t) \approx \alpha(t) \exp\big(j4\pi(f_c + Lt)R(t)/c\big), \tag{3}$$

and outputs the raw ADC data $s[n]$ which is a sampled version of the original BF signal $s(t)$.

After obtaining the sampled BF signals output by the radar, we then aim to extract from them the signal features related to the rotation speed. In Sec. III, we will introduce our proposed signal feature *index of the first peak (IFP)* that bridges the radar signal characteristics and the rotation speed.

III. Rotation Related Feature: IFP

In this section, we introduce the notion of our proposed signal feature IFP, whose relationship with the target object's rotation speed acts as the theoretical foundation of mRotate.

A. IFP Extraction

After obtaining the raw ADC data $s[n]$ of the k-th BF signal, we conduct the *Range-FFT* operation on $s[n]$, which takes FFT on consecutive samples of $s[n]$ to obtain its frequency spectrum, and maps each frequency spectrum component to the discrete range bins. The frequency spectrum component corresponding to the range bin that the ERS-radar distance belongs to is referred to as the *ERS component* F_k, where[1]

$$F_k = \alpha\big((k-1)T_I\big) \exp\big(j4\pi f_c R\big((k-1)T_I\big)/c\big). \tag{4}$$

Clearly, F_k is a sample of a continuous signal $F(t)$ with

$$F(t) = \alpha(t) \exp\big(j4\pi f_c R(t)/c\big). \tag{5}$$

Since the period of $\alpha(t)$ and $R(t)$ equals to the target object's rotation period T, $F(t)$ is also periodic with period T.

To investigate the temporal properties of $F(t)$, we set the radar to consecutively transmit N chirps and obtain the N ERS components[2] $\{F_k\}_{k\in[N]}$, which compose a sampling series of $F(t)$ with a sampling frequency $1/T_I$. We refer to such a series as the *rotation signal series* F'. After obtaining F', we then calculate its *autocorrelation series* X. Specifically, X is a discrete series of length $N-1$, whose p-th value $X[p]$ satisfies

$$X[p] = \frac{1}{N-p} \sum_{n=1}^{N-p} F'[n] \overline{F'}[n+p], \tag{6}$$

[1]Since the duration of a chirp is only around 0.1ms in our experiments, the rotation of the target object can be neglected during this period, and $R(t)$ can be regarded always equal $R((k-1)T_I)$ with $t \in [(k-1)T_I, (k-1)T_I + T_c]$.

[2]We denote $[A] = \{1, 2, \cdots, A\}$ for any positive integer A.

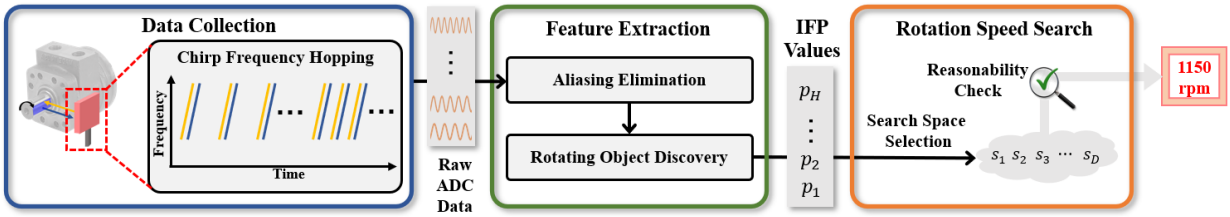

Figure 2: The framework of mRotate.

where $\overline{F'}[n+p]$ is the conjugate of $F'[n+p]$. According to the characteristic of the autocorrelation series, a maximum value of X occurs at index p^* with

$$p^* T_I = mT, \tag{7}$$

where m referred to as the *rotation period coefficient* is any positive integer. We define the smallest p^* that satisfies Eq. (7) as the index of the first peak (IFP).

B. IFP and mRotate

Through the IFP value, we bridge the chirp generation interval T_I and the target object's rotation speed $1/T$ according to Eq. (7). However, in real applications, obtaining the rotation speed from the IFP is anything but trivial. We enumerate the three key challenges of such task as follows.

- In real applications, the range bin that the ERS-radar distance belongs to is *a priori* unknown. *How can we correctly find such range bin to build the autocorrelation series X?*
- As we will show in Sec. IV-B, the aliasing problem makes the IFP overwhelmed in the interferences. *How can we robustly extract the true IFP in such scenario?*
- Even if we obtain the correct value of IFP, according to Eq. (7), we can not directly solve the rotation speed, since the value of the rotation period coefficient m is unknown. *How can we accurately get the rotation speed from the IFP values under multiple choices of rotation period coefficient?*

In Sec. IV, we will introduce the details of mRotate, which solves the above challenges and exploits the properties of IFP to accurately sense the rotation speed.

IV. mRotate Design

In this section, we introduce our design details of mRotate, a mmWave radar-based rotation speed sensing system. As shown in Fig. 2, mRotate consists of the following modules.

- **Data Collection (DC)**. In the DC module, the mmWave radar transmits chirps according to our carefully designed *Chirp Frequency Hopping (CFH)* mechanism. After that, the radar outputs the raw ADC data of the BF signals.
- **Feature Extraction (FE).** The FE module takes the raw ADC data as inputs, and outputs the IFP values. The IFP values are extracted from the raw ADC data by the *Aliasing Elimination (AE)* sub-module and *Rotation Object Discovery (ROD)* sub-module.
- **Rotation Speed Search (RSS)**. The RSS module takes in the IFP values extracted by the FE module and obtains the rotation speed through the *rotation speed search* algorithm.

ALGORITHM 1: Chirp Frequency Hopping.

Input: A group $\mathcal{C} = \{1/T_i\}_{i\in[H]}$ of chirp generation frequencies;
Output: The $H \times N$ groups of raw ADC data $\{s_{i,j}\}_{i\in[H],j\in[N]}$ of BF signals;
1 **foreach** $i \in [H]$ **do**
2 **foreach** $j \in [N]$ **do**
3 The radar transmits the j-th chirp following the chirp generation frequency $1/T_i$;
4 The radar obtains the raw ADC data $s_{i,j}$ of the corresponding BF signal;
5 **return** $\{s_{i,j}\}_{i\in[H],j\in[N]}$;

In the rest of this section, we focus on illustrating the rotation speed sensing for a single object. In Sec. V-D2, we will show that mRotate is able to simultaneously measure multiple objects after straightforward augmentations .

A. Data Collection

In most of the common sensing applications (e.g., motion speed, distance, and material sensing), the mmWave radar transmits a fixed number of chirps in each unit time interval. However, such a chirp generation mechanism is unsuitable for rotation speed sensing for the following reason. We can only extract one IFP value from the chirps generated following a fixed generation frequency. In such case, according to Eq. (7), we cannot directly acquire the T because the value of the rotation period coefficient m is unknown. Actually, we need to extract multiple IFP values under different chirp generation frequencies to build multiple equations in the form of Eq. (7) to solve T. To this end, in the DC module, we propose the CFH mechanism described in Alg. 1.

At first, the algorithm takes a set $\mathcal{C}$ of chirp generation frequencies as input. After that, the radar generates consecutive N chirps following each chirp generation frequency in $\mathcal{C}$ and outputs the corresponding raw ADC data of the BF signals (line 3-4). Finally, the algorithm outputs the $H \times N$ groups of raw ADC data $\{s_{i,j}\}_{i\in[H],j\in[N]}$ (line 5). The obtained raw ADC data will be further utilized by the FE module to extract H IFP values as elaborated in Sec. IV-B.

B. Feature Extraction

1) Challenges of Extracting IFP: In Sec. III, we introduce the basic steps to extract IFP from the raw ADC data. However, in real applications, two key challenges prevent us from acquiring the accurate IFP.

The first challenge is that *the aliasing problem makes it difficult to obtain the true value of IFP*. To illustrate it, we

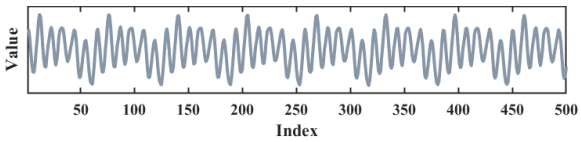

(a) The in-phase components of the rotation signal series F'.

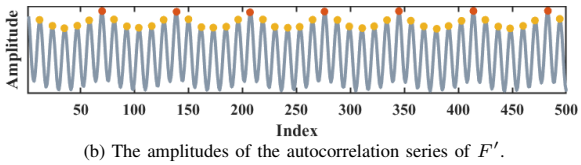

(b) The amplitudes of the autocorrelation series of F'.

Figure 3: The in-phase components of F' in our six-blade fan sensing experiment and its autocorrelation series, with the red points indicating periodic rotation peaks and the yellow points indicating the aliasing peaks.

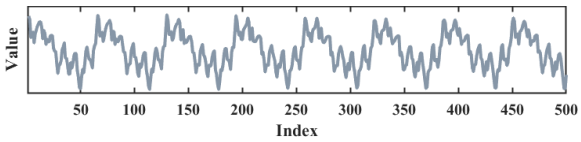

(a) The in-phase components of GSV series.

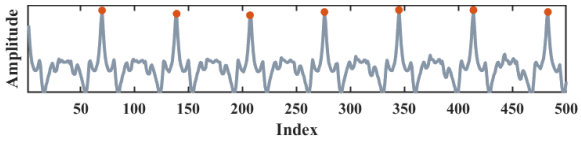

(b) The amplitudes of the autocorrelation series corresponding to the GSV series.

Figure 4: The in-phase components of the GSV series in our six-blade fan sensing experiment and its autocorrelation series, with the red points indicating the periodic rotation peaks.

conduct an experiment that applies the mmWave radar to sense the rotation speed of a six-blade fan. We collect the raw ADC data of 500 consecutive chirps under a fixed chirp generation frequency, and obtain the rotation signal series F' shown in Fig. 3a. The autocorrelation series of F' is plotted in Fig. 3b, which contains the following two kinds of peaks.

- *Periodic rotation peaks*. These peaks are plotted in red dots in Fig. 3b and are caused by the periodic rotation of the target object. The index of the smallest periodic rotation peaks is the IFP and the indices of the remaining rotation peaks are the multiples of the IFP that also satisfy Eq. (7).
- *Aliasing peaks*. Between two consecutive periodic rotation peaks, there are five aliasing peaks plotted in yellow dots in Fig. 3b. Specifically, autocorrelation is a similarity measurement of the original series and its time-lagged version. The centrosymmetric structure of the rotating fan makes the pattern of the signal reflected by each of the fan's six blades highly similar. Such similarity also exists in F', since it is the description of the BF signals in the frequency domain. Thus, the in-phase[3] components of F' shows a "virtual period" which is six times shorter than its true period as shown in Fig. 3a, and five aliasing peaks occur between the two consecutive periodic rotation peaks as shown in Fig. 3b.

As shown in Fig. 3b, since the amplitudes of the aliasing peaks are very close to those of the periodic rotation peaks, we may easily confuse the aliasing peaks with periodic rotation peaks and further obtain the wrong IFP values. Since many rotating objects are roughly centrosymmetric (e.g., wheels, drills, fans), the aliasing problem is a key challenge that influences the accuracy of rotation speed sensing.

The second challenge is that in real practice *the range bin which the ERS-radar distance belongs to is a priori unknown,* which makes it hard to distinguish the signal reflected by the rotating object from the mixed reflection signals to extract IFP.

In the rest of this section, we will introduce the details of the FE module, which solves the above two challenges using the AE and ROD sub-module, respectively.

2) FE Module Overview: The workflow of the FE module is illustrated in Alg. 2. The FE module takes the $H \times N$ groups of raw ADC data $\{s_{i,j}\}_{i\in[H],j\in[N]}$ as inputs and outputs the extracted H IFP values. For each N groups of the raw ADC data obtained under the same chirp generation frequency, the FE module feeds them to the AE sub-module to acquire B aliasing free autocorrelation series (line 2). After that, the obtained B autocorrelation series will be fed into the ROD sub-module to discover the range bin that the ERS-radar distance belongs to and extract the IFP value (line 3). After H iterations, the algorithm outputs the H IFP values (line 4).

ALGORITHM 2: Feature Extraction.

Input: The $H \times N$ groups of the raw ADC data $\{s_{i,j}\}_{i\in[H],j\in[N]}$ of the BF signals;
Output: The H IFP values $\{p_i\}_{i\in[H]}$;
1 **foreach** $i \in [H]$ **do**
  `// Aliasing Elimination.`
2 $\{X_b\}_{b\in[B]} \leftarrow \text{AE}(\{s_{i,j}\}_{j\in[N]})$;
  `// Rotating Object Discovery.`
3 $p_i \leftarrow \text{ROD}(\{X_b\}_{b\in[B]})$;
4 **return** $\{p_i\}_{i\in[H]}$;

3) Aliasing Elimination: As elaborated in Alg. 3, the AE sub-module takes the N groups of raw ADC data $\{s_{i,j}\}_{j\in[N]}$ collected under the chirp generation frequency $1/T_i$ as inputs and outputs the aliasing free autocorrelation series $\{X_b\}_{b\in[B]}$ by our *Chirp Decomposition (CD)* and *Feature Aggregation (FA)* mechanism. At first, the algorithm applies the CD mechanism to decompose each of the sampled BF signals $s_{i,j}$ into K sampled sub-BF signals $\{c_{k,j}\}_{k\in[K]}$ (line 2). After that, the algorithm applies the FA mechanism to generate the *group sum values (GSVs)* from the sampled sub-BF signals for aliasing free autocorrelation series calculation (line 3-6). After the normalization process (line 7-8), the algorithm calculates the autocorrelation series of the GSVs (line 9-10) and outputs the aliasing free autocorrelation series $\{X_b\}_{b\in[B]}$ (line 11).

Chirp Decomposition. As discussed in Sec. IV-B1, the ERS components of the chirps that measure the centrosymmetric parts of the rotating object are similar, which incurs the aliasing peaks in the autocorrelation series. Our first step to relieve this problem is to *find more ERS components to provide richer information of the rotation* through the CD mechanism.

According to Eq. (4), the phase of the ERS component is determined by both the chirp starting frequency f_c and ERS-radar distance. If the radar could simultaneously generate mul-

[3]We omit the quadrature components of F' for conciseness because they show similar trends as in-phase components.

ALGORITHM 3: Aliasing Elimination.

Input: The N groups of raw ADC data $\{s_{i,j}\}_{j\in[N]}$ collected under chirp generation frequency $1/T_i$;
Output: The B autocorrelation series $\{X_b\}_{b\in[B]}$;

1 **foreach** $j \in [N]$ **do**
  // Chirp Decomposition.
2 $\{c_{k,j}\}_{k\in[K]} \leftarrow$ Decompose$(s_{i,j})$;
  // Feature Aggregation.
3 **foreach** $k \in [K]$ **do**
4 $T_{k,j} \leftarrow$ Range-FFT$(c_{k,j})$;
5 **foreach** $b \in [B]$ **do**
6 $G_{b,j} \leftarrow \sum_{k=1}^{K} T_{k,j}[b]$;
7 **foreach** $b \in [B]$ **do**
8 $G_{b,j} \leftarrow G_{b,j} - 1/n \sum_{h=1}^{N} G_{b,h}$;
  // Generate autocorrelation series.
9 **foreach** $b \in [B]$ **do**
10 $X_b \leftarrow$ Autocorrelation$(\{G_{b,j}\}_{j\in[N]})$;
11 **return** $\{X_b\}_{b\in[B]}$;

tiple chirps with different starting frequencies, we could get multiple ERS components whose phases are the descriptions of the ERS-radar distance under different starting frequencies. Thus, our CD mechanism decomposes each chirp into K sub-chirps[4] (line 2 in Alg. 3). As illustrated in Fig. 5, a sub-chirp is a consecutive portion of the original chirp, whose corresponding sub-BF signal contains a consecutive portion of the original BF signal. Since the duration of a chirp is only around 0.1ms, we deem the object's rotation negligible during this period and all the sub-chirps are simultaneously generated.

Actually, the hardware of our mmWave radar itself does not support chirp decomposition. The CD mechanism can be equivalently achieved by directly decomposing the original BF signals into sub-BF signals, which in practice is realized by dividing the raw ADC data of the original BF signal into multiple segments, as illustrated in Fig. 5.

Feature Aggregation. After obtaining multiple sub-chirps, we propose to aggregate the obtained signal features from the sub-chirps to generate a new signal feature, which distinctly amplifies the tiny differences between the centrosymmetric parts of the rotating object. Specifically, after decomposing the sampled BF signal $s_{i,j}$ into K sampled sub-BF signals $\{c_{k,j}\}_{k\in[K]}$ (line 2 in Alg. 3), we conduct Range-FFT on each $c_{k,j}$ and obtain K corresponding Range-FFT series denoted as $\{T_{k,j}\}_{k\in[K]}$ (line 4 in Alg. 3), where each Range-FFT series $T_{k,j}$ is a $B\times 1$ vector with B denoting the total number of the range bins. The GSV $G_{b,j} = \sum_{k=1}^{K} T_{k,j}[b]$ for each $b \in [B]$ is extracted by adding up the all the components with the same index[5] b in $\{T_{k,j}\}_{k\in[K]}$ (line 6 in Alg. 3).

Actually, suppose the ERS-radar distance belongs to the r-th range bin, then the elements in $\{T_{k,j}[r]\}_{k\in[K]}$ are the ERS components of the corresponding K sub-chirps. For different centrosymmetric parts of the rotating object, the differences of their corresponding GSVs are larger than the differences

[4]A larger K leads to more ERS components with increased computational cost, and we set K empirically in our experiments as given in Sec. V-C2.

[5]We denote the b-th value of a $B \times 1$ vector Y as $Y[b]$.

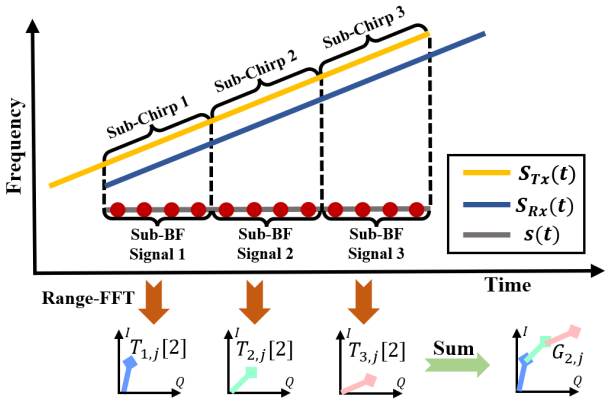

Figure 5: The illustration of CD and FA mechanism. The red dots indicate the samples of the BF signal. Here we decompose a chirp into three sub-chirps and calculate the GSV for the second value in each Range-FFT series.

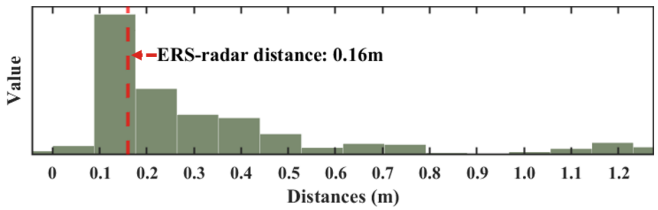

Figure 6: The maximum values in autocorrelation series of the GSVs in each range bin, and the ERS-radar distance, in our six-blade fan sensing experiment.

of their ERS components. This is because the difference of the two GSVs G_{r,j_1} and G_{r,j_2} is the cumulative difference of $\{T_{k,j_1}[r]\}_{k\in[K]}$ and $\{T_{k,j_2}[r]\}_{k\in[K]}$. In Fig. 4a, we plot the $G_{r,j}$ series extracted from the raw ADC data collected in the six-blade fan sensing experiment mentioned in Sec. IV-B1. Compared with the series of ERS components shown in Fig. 3a, the similarity between the GSVs corresponding to the rotating object's different centrosymmetric parts is greatly reduced. The aliasing peaks in the autocorrelation series of $G_{r,j}$ are also eliminated as shown in Fig. 4b.

Since we have no prior knowledge about the range bin that the ERS-radar distance belongs to, Alg. 3 calculates the autocorrelation series of GSVs for all the B range bins (line 11) and leaves the ERS-radar distance's range bin discovery task to the following ROD sub-module.

4) Rotating Object Discovery: The ROD sub-module takes the B autocorrelation series output by the AE sub-module as inputs, and outputs the extracted IFP. The ROD sub-modue solves the key challenge of discovering the range bin that the ERS-radar distance belongs to by utilizing the periodically varying pattern of the rotating object's reflected signal. Note that such characteristics also remain in the extracted GSVs. Moreover, only the autocorrelation series of a periodic series have distinct large values. In Fig. 6, we plot the maximum values in the autocorrelation series of the GSVs in all the B range bins, which are extracted from the data collected in the six-blade fan sensing experiment mentioned in Sec. IV-B1. We notice that the maximum value of the autocorrelation series corresponding to the range bin that the ERS-radar distance belongs to is distinctly larger than others.

The detailed workflow of the ROD sub-module is elaborated in Alg. 4. After initialization (line 1), the algorithm calculates

ALGORITHM 4: Rotation Object Discovery.

Input: The B autocorrelation series $\{X_b\}_{b\in[B]}$;
Output: The IFP value p;
// Initialization.
1 $I \leftarrow$ empty array, $\mathcal{I} \leftarrow \emptyset$;
2 **foreach** $b \in [B]$ **do**
3 $\quad v_b \leftarrow \max_{n\in[N-1]} X_b[n]$;
// Find the rotating object's range bin.
4 $q \leftarrow \arg\max_{b\in[B]} v_b$;
// Calculate the IFP value.
5 **foreach** $j \in [N-1]$ **do**
6 $\quad$ **if** $X_q[j] > \eta v_q$ **then**
7 $\quad\quad$ Insert j to the end of I;
8 **foreach** $i \in [\text{length}(I)-1]$ **do**
9 $\quad \mathcal{I} \leftarrow \mathcal{I} \bigcup \{I[i+1] - I[i]\}$;
10 $p \leftarrow \text{mode}(\mathcal{I})$;
11 **return** p;

the maximum value of each autocorrelation series (line 2-3), and picks the autocorrelation series X_q with the largest maximum value, whose corresponding range bin is the one that the ERS-radar distance belongs to (line 4). After that, the algorithm collects in an array I the indices of the periodic rotation peaks in X_q (line 5-7). Specifically, an index j is selected into I only if the indexed value $X_q[j]$ is close to[6] v_q (line 6). The IFP value is calculated as the mode of the distances between the consecutive indices of the periodic rotation peaks (line 8-10). Compared with setting the smallest element in I as the IFP, such a mechanism improves the reliability of the results because the IFP can be accurately obtained as long as the majority of the indices in I are correct. Finally, the algorithm outputs the IFP p (line 11).

C. Rotation Speed Search

After receiving the IFP values generated by the FE module, the RSS module elaborated in Alg. 5 outputs the object's rotation speed. At first, the algorithm initializes (line 1) the rotation speed s and the variable d which will be used for checking the reasonableness of the candidate rotation speeds. According to Eq. (7), the H IFP values $\{p_i\}_{i\in[H]}$ and their corresponding chirp generation frequencies $\{1/T_i\}_{i\in[H]}$ satisfy

$$p_i T_i = m_i T, \quad \forall i \in [H], \tag{8}$$

where $\{m_i\}_{i\in[H]}$ are the rotation period coefficients whose values are unknown positive integers. In other words, each $p_i T_i$ must be an integral multiple of the rotation period T. Moreover, since the chirp generation frequency of our mmWave radar is higher than the target object's rotation speed[7] $1/T$, the value of T must be in the set $\{p_i T_i/m\}_{m\in[p_i]}$. Thus, the algorithm then finds the minimum search space for the least computational cost (line 2).

After that, for each calculated candidate rotation period T in the search space $\{DT_i/m\}_{m\in[D]}$ (line 4), the algorithm checks whether T satisfies two groups of conditions (line 5-14). The algorithm calculates the rotation period coefficients[8] $\{r'_j\}_{j\in[H]}$ (line 5-6) under each chirp generation frequency in $\mathcal{C}$, and checks the first group of the conditions that whether the elements in $\{p_j\}_{j\in[H]}$ are still the IFPs, if the target object's rotation period is T (line 7-10). The algorithm introduces a boolean variable u to indicate whether the current T passes the IFP check, and initializes u as True (line 7). If the condition[9] in line 9 holds, the IFP value under the chirp generation frequency $1/T_j$ should be $p_j/\text{GCD}(r'_j, p_j)$ rather than p_j according to Eq. (8), where r'_j is the calculated rotation period coefficient and p_j is the extracted IFP value under the chirp generation frequency $1/T_j$. In such case, the current T does not pass the IFP check, and the algorithm sets u as False (line 10). If T passes the IFP check, the algorithm further checks it for the second groups of conditions (line 12-14). According to Eq. (8), the rotation period T should satisfy that

$$p_i T_i \bmod T = 0, \quad \forall i \in [H]. \tag{9}$$

If Eq. (9) holds, all the r_j's calculated in line 6 should be integers and the value of w in line 12 will be 0. However, due to the signal noise of the raw ADC data in real-world measurements, Eq. (9) may not hold for all the H measurements. Thus, the algorithm uses the variable d to record the minimum value of w so far, and updates the rotation speed value as $s = 1/T$, if d is updated (line 13-14). The rotation period T with the smallest w is most likely to satisfy Eq. (9). Finally, the algorithm outputs the rotation speed s (line 15).

ALGORITHM 5: Rotation Speed Search.

Input: The set of chirp generation frequencies $\mathcal{C} = \{1/T_i\}_{i\in[H]}$ and IFP values $\{p_i\}_{i\in[H]}$;
Output: The object's rotation speed s;
// Initialization.
1 $s \leftarrow 0$, $d \leftarrow H+1$;
// Decide the rotation period search space.
2 $D \leftarrow \min_{i\in[H]} p_i$;
// Search the rotation period.
3 **foreach** $m \in [D]$ **do**
4 $\quad T \leftarrow DT_i/m$;
$\quad$ // Satisfaction check for IFPs.
5 $\quad$ **foreach** $j \in [H]$ **do**
6 $\quad\quad r_j \leftarrow p_j T_j/T$, $r'_j = \text{round}(r_j)$;
7 $\quad u \leftarrow$ True;
8 $\quad$ **foreach** $j \in [H]$ **do**
9 $\quad\quad$ **if** $\text{GCD}(r'_j, p_j) > 1$ **then**
10 $\quad\quad\quad u \leftarrow$ False;
$\quad$ // Satisfaction check for Eq. (9).
11 $\quad$ **if** $u =$ True **then**
12 $\quad\quad w \leftarrow \sum_{j=1}^{H} |r_j - r'_j|$;
13 $\quad\quad$ **if** $d < w$ **then**
14 $\quad\quad\quad d \leftarrow w$, $s \leftarrow 1/T$;
15 **return** s;

[6]Note that $\eta < 1$ and η is close to 1.

[7]The chirp generation frequency of our mmWave radar is as high as 1e3Hz, which is much higher than the rotation speed of common objects.

[8]The round(x) in line 6 of Alg.5 is to obtain the nearest integer of x.

[9]The GCD$(\cdot,\cdot)$ in line 9 is to calculate the greatest common divisor between two values.

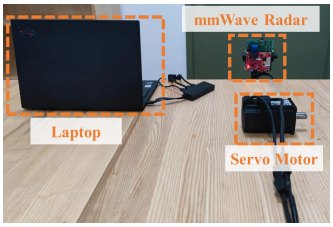

Figure 7: Servo motor.

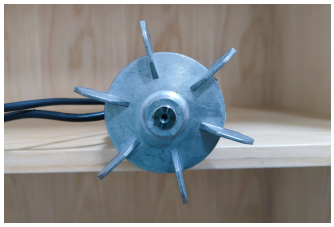

Figure 8: Six-blade fan on servo motor.

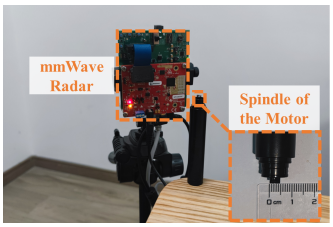

Figure 9: Tiny motor spindle.

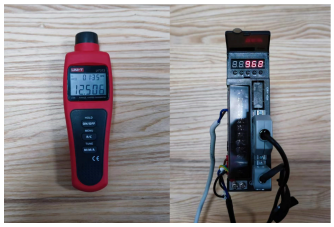

Figure 10: Laser tachometer (left) and electromagnetic tachometer (right).

Figure 11: CNC machining center.

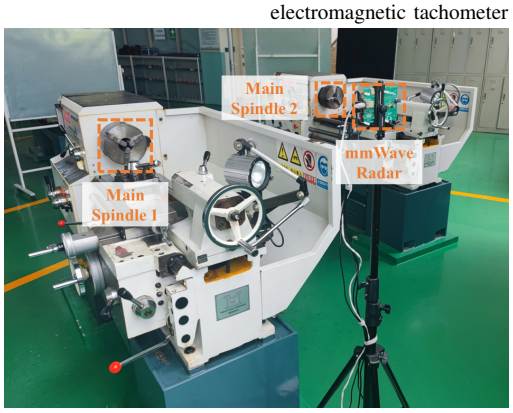

Figure 12: Two turning lathes.

V. Evaluation

A. Implementation and Experimental Setup

1) Implementation: We implement mRotate with a commercial mmWave radar TI IWR1443 BoosterPack [14]. The raw ADC data is collected by a TI DCA1000EVM data acquisition board [15]. The data processing codes are written in Matlab and run on a computer with Intel Core i7-1160G7 processor and 16GB memory.

2) Experiment Setting: We conduct extensive experiments to evaluate the performance of mRotate. The experiment settings in lab environments include the following **setting 1** with a servo motor whose rotation speed can be flexibly designated shown in Fig. 7 to evaluate the sensing accuracy and sensing distance, **setting 2** with a six-blade fan attached on the servo motor shown in Fig. 8 to evaluate the centrosymmetric object sensing performance, and **setting 3** with a tiny motor spindle shown in Fig. 9 to evaluate the tiny object sensing performance. The experiment settings for field tests in a machining workshop include **setting 4** on a computerized numerical control (CNC) machining center shown in Fig. 11 to validate that mRotate can accurately sense the rotation speeds of a large mechanical device, and **setting 5** on the main spindles of two turning lathes shown in Fig. 12 to validate that mRotate can measure the rotation speeds of multiple devices.

3) Baseline and Ground Truth: The baseline which we compare mRotate with is a commercial laser tachometer UNI-T UT372 [13] shown in Fig. 10. Note that if we operate the laser tachometer to sense the rotation speed of the servo motor by sticking its reflective tag on the spindle as recommended in its manual, the laser tachometer will fail, because the metal spindle provides strong reflection which overwhelms the laser pulses reflected by the tag. Thus, we have to cover the spindle with black paper and then stick the reflective tag on it.

The ground truth of the servo motor and the fan is obtained by the accurate build-in motor electromagnetic tachometer shown in Fig. 10. For the tiny motor spindle, we use the measurement result of the laser tachometer as the ground truth, since it shows good performance on high-speed sensing, as we will discuss in Sec. V-B. In field tests, the ground truth is obtained by designating (for the CNC machining center) or reading from the nameplates (for the turning lathes).

B. Rotation Speed Sensing Accuracy

In setting 1, we set 25 levels of the servo motor rotation speeds evenly spanning from 100rpm to 2300rpm, and set the motor spindle-radar distance as 50cm. The absolute percentage errors[10] (APE) of mRotate and laser tachometer under different rotation speeds are shown in Fig. 13. mRotate achieves a lower mean absolute percentage error (MAPE) (0.24%) than the laser tachometer (0.39%). The laser tachometer obtains high errors when the rotation speed is low, because in such case one bit error of the laser pulse counts will cause high APE. However, mRotate obtains low APE in such case thanks to that the CFH mechanism provides multiple measurements and the RSS algorithm robustly searches the accurate rotation speed by utilizing all the measurement results.

C. Impact of Practical Factors

1) Measurement Distance: The measurement distance is of great importance for the safety of the operators. In setting 1, we evaluate the impact of the measurement distance of mRotate. We first place the mmWave radar 0.5m, 1m, 1.5m, 2m, and 2.5m away from the spindle of the servo motor. For each spindle-radar distance, we set the rotation speed as three

[10]Suppose v_s is the sensing value and v_g is the ground truth value, the absolute percentage error is $|v_g - v_s|/v_g$.

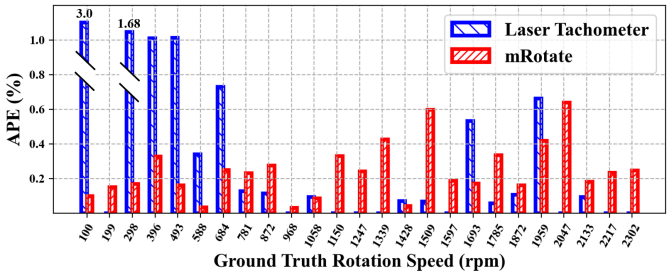

Figure 13: The APEs of mRotate and the laser tachometer under different rotation speeds for experiments in setting 1.

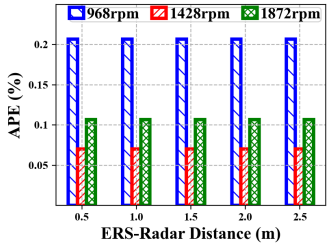

Figure 14: The APEs of mRotate under different measurement distances and rotation speeds in setting 1.

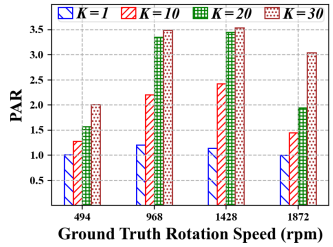

Figure 15: The PARs with different sub-chirp numbers and rotation speeds for experiments in setting 2.

speed levels 968rpm, 1428rpm, and 1872rpm which distribute evenly from around 1000rpm to 2000rpm. As shown in Fig. 14, mRotate achieves an APE lower than 0.21% for all the measurements, and the APE is stable against the increasing distances. This experiment validates that mRotate is able to accurately measure the rotation speed from as far as 2.5m.

2) Centrosymmetric Rotating Object Measurement: In setting 2, we evaluate mRotate to sense a centrosymmetric rotating object. As shown in Fig. 8, we attach a six-blade fan on the servo motor, and set eight levels of the rotation speeds which distribute evenly from around 250rpm to 2000rpm. The fan-radar distance is 16cm. We compare the results of mRotate with or without the AE mechanism in Tab. I. Without the AE mechanism, mRotate is badly affected by the aliasing problem and its sensing results are four to six times higher than the ground truth. In contrast, with the AE mechanism, mRotate achieves an APE lower than 0.24% for all the measurements.

To further investigate the influence of the number of sub-chirps on the functionality of the AE mechanism, we plot in Fig. 15 the PARs[11] of the autocorrelation series, which are generated from the GSVs series aggregated from different number of sub-chirps. We show the results under four rotation speed levels (i.e., 494rpm, 968rpm, 1428rpm, 1872rpm) for conciseness because the results under the other four speed levels in Tab. I show similar trends. We notice that without the AE mechanism (i.e., the number of sub-chirps is 1), the PAR is very close to 1. As we use more sub-chirps, the PAR is becoming larger and the differences between the periodic rotation peaks and aliasing peaks are amplified. In all the experiments, we set the number of sub-chirps as 30, because such a configuration is both computationally efficient and easy to distinguish the periodic rotation peaks and aliasing peaks.

[11]PAR is the ratio of the periodic rotation peaks' mean amplitude and the aliasing peaks' mean amplitude.

Table I: Comparison of mRotate with or without AE in setting 2. The unit of the numbers in the table is rpm.

Ground Truth	250	493	733	968	1202	1428	1640	1872
with AE	250	494	732	968	1200	1429	1644	1875
without AE	1550	2927	4127	5714	7059	8577	9864	10909

Table II: Ground truths and the measurement results of mRotate for field tests. The unit of the numbers in the table is rpm.

Devices	CNC Machining Center					Turning Lathe 1	Turning Lathe 2
Ground Truth	1000	2000	3000	4000	5000	560	1120
mRotate	1001	2000	3003	4000	5000	563	1111

3) Target Object Size: To investigate mRotate's ability to measure the rotation speed of tiny objects, in setting 3, we evaluate mRotate on a tiny motor spindle. As illustrated in Fig. 9, the width of the spindle is only 5mm. We set the spindle-radar distance as 10cm. The rotation speed measurement result of mRotate is 12500rpm, and the APE is only 0.34%. This experiment validates that mRotate can accurately measure the rotation speed of an object with (i) a small size (several millimeters) and (ii) a rotation speed as high as 12500rpm.

D. Field Tests

1) Measurement for Multiple Speed Levels: In setting 4, we evaluate mRotate on a high-end CNC machining center, as shown in Fig. 11. We set 5 levels of rotation speeds which distribute evenly from 1000rpm to 5000rpm. Tab. II shows that mRotate achieves high rotation speed sensing accuracy (APE $\leq 0.1\%$) in all the 5 speed levels. The distance between the machine drill and the protection baffle is 0.75m, which is far beyond the laser tachometer's recommended operation distance ($<$ 20cm). However, mRotate can accurately sense the machine drill from a distance of as far as around 1m.

To further illustrate the effectiveness of the ROD mechanism for discovering the rotating object's range bin in complex real-world environments, we plot the ERS-radar distance, the maximum values of autocorrelation series of GSVs in each range bin, and the Range-FFT series in Fig. 16 and Fig. 17. The traditional object detection approach which searches for the peaks in the Range-FFT series cannot distinguish the rotating object. However, the ROD mechanism can accurately discover the ERS-radar distance by utilizing the distinctly large maximum value of the rotating object's corresponding autocorrelation series of the GSVs.

2) Multi-object Measurement: Thanks to the wide field of the view (FoV) of our mmWave radar[12], mRotate can simultaneously measure the rotation speeds of multiple objects. In setting 5, we evaluate the performance of mRotate for sensing the rotating speeds of the main spindles of two turning lathes as illustrated in Fig. 12.

We first introduce how mRotate simultaneously senses the rotation speeds of multiple objects. We plot in Fig. 18 and Fig. 19 the ERS-radar distances, the maximum values of autocorrelation series of GSVs in each range bin, and the Range-FFT series in setting 5. As shown in Fig. 19, it is

[12]110° azimuth FoV and 30° elevation FoV.

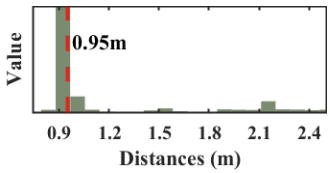

Figure 16: The maximum values of autocorrelation series of GSVs in each range bin for experiments in setting 4.

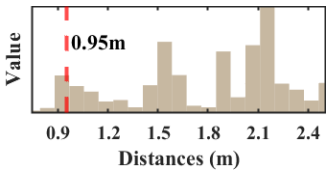

Figure 17: The Range-FFT series of sampled sub-BF signal for experiments in setting 4.

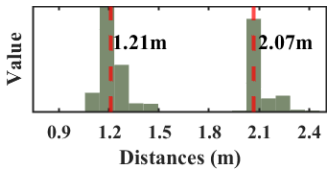

Figure 18: The maximum values of autocorrelation series of GSVs in each range bin for experiments in setting 5.

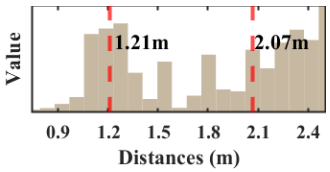

Figure 19: The Range-FFT series of sampled sub-BF signal for experiments in setting 5.

difficult to distinguish the rotating objects by searching for the peaks in Range-FFT series, while in Fig. 18 the maximum value of the autocorrelation series corresponding to the range bins that the two rotating objects' ERS-radar distances belong to are distinctly larger than the others. To enable multiple objects' rotation speed sensing, we thus slightly change the ROD sub-module introduced in Sec. IV-B4 to pick out the multiple autocorrelation series by setting a threshold on their maximum values. After that, we extract the IFP values and search the rotation speeds of the multiple rotating objects.

As shown in Tab. II, mRotate can simultaneously sense the rotation speed of the two main spindles in setting 5 with a high accuracy (APE $\leq 0.8\%$ for both the two main spindles).

VI. Related Work

Rotation speed sensing. Existing works on rotation speed sensing can be categorized as *contact-based* and *contactless* approaches. The contact-based sensors [4] are physically attached to the shaft of the target object. Such a measurement mode constrains their operation distances, which is likely to cause safety risks to the operator. The contactless approaches relieve this problem and have become promising paradigms for rotation speed sensing. The contactless approaches can be categorized as electromagnetic-based [5, 6], optical-based [7–13], and RF-based ones [16, 17].

The electromagnetic-based methods utilize electrostatic [5] or hall-effect [6] sensors to detect the change of the electromagnetic field caused by the object's rotation. Although the electromagnetic-based methods enable contactless measurement, their operation distances are less than 10cm.

The optical-based approaches utilize a variety of optical sensors for rotation speed sensing. Among them, [7, 8] utilize RGB cameras to capture the images of the rotating object and estimate the object's rotation speed by analysing the extracted features of the images. However, these approaches can only measure rotation speeds less than 1500rpm, constrained by the relatively low frame rate (30 fps) of the RGB cameras. Other works also propose to use high-speed cameras [9–12] to enlarge the measurement range of the rotation speed. However, the prohibitive prices of these cameras prevent them from being broadly adopted. Besides, all the above camera-based approaches fail to operate under poor illuminations. The laser tachometers [13] are robust to illumination conditions. However, the laser tachometer fail if the target object itself is highly reflective. In such case, the laser tachometer cannot distinguish the laser pulse reflected by its reflective tag from those reflected by the object. Besides, the operation distance of the laser tachometer (around 20cm [13]) is also inadequate for many applications that require a longer safe distance.

Table III: Comparison with other rotation speed sensing methods.

Method	Safe Sensing Range	Object Independent	Illumination Independent	Require Training
Mechanical [4]	no	yes	yes	no
Electromagnetic [5, 6]	no	no	yes	no
Camera [7–12]	yes	yes	no	no
Laser [13]	no	no	yes	no
SpiralSpy [16]	yes	no	yes	yes
RFTacho [17]	no	yes	yes	yes
mRotate	**yes**	**yes**	**yes**	**no**

Compared with the above contactless approaches, mRotate employs the RF signal for rotation speed sensing from a reasonable distance, and is robust to the illumination conditions and the target object's light reflectivity. Note that [16] also utilizes mmWave radar for fan rotation speed sensing. However, the method proposed in [16] requires training, and does not support sensing other objects and the rotation speed out of the labels in training dataset. The method proposed in [17] has a maximum sensing distance of around 65cm, which is inadequate for safely measuring the rotation speed of many types of industrial machines. We comprehensively compare mRotate with the above methods in Tab. III.

mmWave-based sensing. Apart from rotation speed sensing, mmWave-based sensing has shown a rising popularity among a lot of other applications, such as micro-displacement sensing [18, 19], vital signs recovery [20–22], posture and gesture sensing [23–28], eavesdropping [29], physical layer attacking [30], and many others [31–41]. Our work distinguishes from the above works, as we leverage the mmWave radar for a different task of rotation speed sensing.

VII. Conclusion

In this paper, we propose mRotate, a mmWave radar-based rotation speed sensing system. Specifically, we design a series of novel approaches that enable mRotate to extract the signal reflected by the rotating object from the mixed reflection signals, generate the aliasing free signal features to enable accurate rotation speed sensing for centrosymmetric objects, and accurately pinpoint the rotation speed through customized radar sensing mode and algorithm design. We extensively evaluate mRotate in both lab environments and field tests. mRotate achieves an MAPE of only 0.24% for accuracy test, which is 38% lower than that produced by the baseline device, a popular commercial laser tachometer. Meanwhile, mRotate can measure the rotation speed of a small spindle whose diameter is only 5mm, achieve low errors from a distance as far as 2.5m, and simultaneously obtain the accurate rotation speeds of multiple objects in field tests.

REFERENCES

[1] Uwoodcraft, "Turning lathe speeds," https://uwoodcraft.com/woodturning-lathe-speeds-a-complete-guide/.

[2] Haynes, "Vehicle inspections," https://haynes.com/en-us/tips-tutorials/what-know-about-vehicle-inspections-all-50-states.

[3] "Rpm in washing machine," https://theportablelaundry.com/washing-machine-rpm/.

[4] REED Instruments, "Photo-contact tachometer instruction manual," https://www.reedinstruments.com/pdfs/cache/www.reedinstruments.com/r7100/manual/r7100-manual.pdf.

[5] L. Li, H. Hu, Y. Qin, and K. Tang, "Digital approach to rotational speed measurement using an electrostatic sensor," *Sensors*, vol. 19, no. 11, 2019.

[6] K. J, B. Varghese, U. A. Ponnary, F. Kamar, and R. T. Jacob, "Hall effect sensor based portable tachometer for rpm measurement," *International Journal of Computer Science and Engineering Communications*, vol. 2, no. 1, pp. 100–105, 2014.

[7] Y. Wang, L. Wang, and Y. Yan, "Rotational speed measurement through digital imaging and image processing," in *2017 IEEE International Instrumentation and Measurement Technology Conference (I2MTC)*, 2017.

[8] T. Wang, Y. Yan, L. Wang, and Y. Hu, "Rotational speed measurement through image similarity evaluation and spectral analysis," *IEEE Access*, vol. 6, pp. 46 718–46 730, 2018.

[9] H. Kim, Y. Yamakawa, T. Senoo, and M. Ishikawa, "Visual encoder: robust and precise measurement method of rotation angle via high-speed rgb vision," *Optics Express*, vol. 24, no. 12, pp. 13 375–86, 2016.

[10] F. Natili, F. Castellani, D. Astolfi, and M. Becchetti, "Video-tachometer methodology for wind turbine rotor speed measurement," *Sensors*, vol. 20, no. 24, 2020.

[11] X. Zhu and S. Yu, "Measurement angular velocity based on video technology," in *The 4th International Congress on Image and Signal Processing (ICSIP)*, 2011.

[12] J. Zhong, S. Zhong, Q. Zhang, and Z. Peng, "Measurement of instantaneous rotational speed using double-sine-varying-density fringe pattern," *Mechanical Systems and Signal Processing*, vol. 103, pp. 117–130, 2018.

[13] U.-T. Technology, "Laser tachometer operating manual," https://meters.uni-trend.com/product/ut370-series/#Docs/.

[14] Texas Instruments Incorporated, "Single-chip 76-ghz to 81-ghz mmwave sensor integrating dsp and mcu," https://www.ti.com/product/IWR1642/.

[15] Texas Instruments Incorporated, "Real-time data-capture adapter for radar sensing evaluation module," http://www.ti.com/tool/DCA1000EVM/.

[16] Z. Li, B. Chen, X. Chen, H. Li, C. Xu, F. Lin, C. X. Lu, K. Ren, and W. Xu, "Spiralspy: Exploring a stealthy and practical covert channel to attack air-gapped computing devices via mmwave sensing," in *The Network and Distributed System Security (NDSS)*, 2022.

[17] M. Heggo, L. Bhatia, and J. A. McCann, "Rftacho: Non-intrusive RF monitoring of rotating machines," in *The 21st International Conference on Information Processing in Sensor Networks (IPSN)*, 2022.

[18] J. Guo, M. Jin, Y. He, W. Wang, and Y. Liu, "Dancing waltz with ghosts: Measuring sub-mm-level 2d rotor orbit with a single mmwave radar," in *The 20th International Conference on Information Processing in Sensor Networks (IPSN)*, 2021.

[19] C. Jiang, J. Guo, Y. He, M. Jin, S. Li, and Y. Liu, "mmvib: micrometer-level vibration measurement with mmwave radar," in *The 26th Annual International Conference on Mobile Computing and Networking (MobiCom)*, 2020.

[20] S. Zhang, T. Zheng, Z. Chen, and J. Luo, "Can we obtain fine-grained heartbeat waveform via contact-free rf-sensing?" in *The 41st International IEEE Conference on Computer Communications (INFOCOM)*, 2022.

[21] Z. Chen, T. Zheng, C. Cai, and J. Luo, "Movi-fi: motion-robust vital signs waveform recovery via deep interpreted RF sensing," in *The 27th Annual International Conference on Mobile Computing and Networking (MobiCom)*, 2021.

[22] X. Xu, J. Yu, C. Ma, Y. Ren, H. Liu, Y. Zhu, Y.-C. Chen, and F. Tang, "mmECG: monitoring human cardiac cycle in driving environments leveraging millimeter wave," in *The 41st International IEEE Conference on Computer Communications (INFOCOM)*, 2022.

[23] H. Kong, X. Xu, J. Yu, Q. Chen, C. Ma, Y. Chen, and L. Kong, "m^3track: mmwave-based multi-user 3d posture tracking," in *The 20th Annual International Conference on Mobile Systems (MobiSys)*, 2022.

[24] H. Xue, Y. Ju, C. Miao, Y. Wang, S. Wang, A. Zhang, and L. Su, "mmmesh: towards 3d real-time dynamic human mesh construction using millimeter-wave," in *The 19th Annual International Conference on Mobile Systems (MobiSys)*, 2021.

[25] S. Palipana, D. Salami, L. A. Leiva, and S. Sigg, "Pantomime: Mid-air gesture recognition with sparse millimeter-wave radar point clouds," *Proceedings of the ACM on Interactive, Mobile, Wearable and Ubiquitous Technologies*, vol. 5, no. 1, pp. 27:1–27:27, 2021.

[26] C. Shi, L. Lu, J. Liu, Y. Wang, Y. Chen, and J. Yu, "mpose: Environment- and subject-agnostic 3d skeleton posture reconstruction leveraging a single mmwave device," *Smart Health*, vol. 23, p. 100228, 2022.

[27] A. Adhikari, S. Avula, and S. Sur, "Mmsleep: Monitoring sleep posture from commodity millimeter-wave devices," in *The 20th Annual International Conference on Mobile Systems (MobiSys)*, 2022.

[28] E. M. Sitar, M. S. Saadat, and S. Sur, "A millimeter-wave wireless sensing approach for at-home exercise recognition," in *The 20th Annual International Conference on Mobile Systems (MobiSys)*, 2022.

[29] P. Hu, Y. Ma, P. S. Santhalingam, P. H. Pathak, and X. Cheng, "MILLIEAR: millimeter-wave acoustic eavesdropping with unconstrained vocabulary," in *The 41st International IEEE Conference on Computer Communications (INFOCOM)*, 2022.

[30] Z. Sun, S. Balakrishnan, L. Su, A. Bhuyan, P. Wang, and C. Qiao, "Who is in control? practical physical layer attack and defense for mmwave-based sensing in autonomous vehicles," *IEEE Transactions on Information Forensics and Security*, vol. 16, pp. 3199–3214, 2021.

[31] C. X. Lu, S. Rosa, P. Zhao, B. Wang, C. Chen, J. A. Stankovic, N. Trigoni, and A. Markham, "See through smoke: Robust indoor mapping with low-cost mmwave radar," in *The 18th Annual International Conference on Mobile Systems (MobiSys)*, 2020.

[32] C. Xu, Z. Li, H. Zhang, A. S. Rathore, H. Li, C. Song, K. Wang, and W. Xu, "Waveear: Exploring a mmwave-based noise-resistant speech sensing for voice-user interface," in *The 17th Annual International Conference on Mobile Systems (MobiSys)*, 2019.

[33] C. X. Lu, M. R. U. Saputra, P. Zhao, Y. Almalioglu, P. P. B. de Gusmao, C. Chen, K. Sun, N. Trigoni, and A. Markham, "Milliego: Single-chip mmwave radar aided egomotion estimation via deep sensor fusion," in *The 18th Conference on Embedded Networked Sensor Systems (SenSys)*, 2020.

[34] J. Pegoraro, J. O. Lacruz, M. Rossi, and J. Widmer, "SPARCS: A sparse recovery approach for integrated communication and human sensing in mmwave systems," in *The 21st International Conference on Information Processing in Sensor Networks (IPSN)*, 2022.

[35] A. B. Pizarro, P. J. Mateo, F. Gringoli, and J. Widmer, "Augmenting mmwave localization accuracy through sub-6 ghz on off-the-shelf devices," in *The 20th Annual International Conference on Mobile Systems (MobiSys)*, 2022.

[36] S. Ding, Z. Chen, T. Zheng, and J. Luo, "Rf-net: a unified meta-learning framework for rf-enabled one-shot human activity recognition," in *The 18th Conference on Embedded Networked Sensor Systems (SenSys)*, 2020.

[37] T. Zheng, Z. Chen, J. Luo, L. Ke, C. Zhao, and Y. Yang, "Siwa: see into walls via deep UWB radar," in *The 27th Annual International Conference on Mobile Computing and Networking (MobiCom)*, 2021.

[38] R. Tavasoli, S. Sur, and S. Nelakuditi, "Sscense: A millimeter-wave sensing approach for estimating soluble sugar content of fruits," in *The 20th Annual International Conference on Mobile Systems (MobiSys)*, 2022.

[39] J. M. Schellberg and S. Sur, "Accurate device self-tracking for robust millimeter-wave imaging on handheld smart devices," in *The 20th Annual International Conference on Mobile Systems (MobiSys)*, 2022.

[40] T. Liu, M. Gao, F. Lin, C. Wang, Z. Ba, J. Han, W. Xu, and K. Ren, "Wavoice: A noise-resistant multi-modal speech recognition system fusing mmwave and audio signals," in *The 19th Conference on Embedded Networked Sensor Systems (SenSys)*, 2021.

[41] E. Soltanaghaei, A. Prabhakara, A. Balanuta, M. Anderson, J. M. Rabaey, S. Kumar, and A. Rowe, "Millimetro: Mmwave retro-reflective tags for accurate, long range localization," in *The 27th Annual International Conference on Mobile Computing and Networking (MobiCom)*, 2021.